American Mineralogist, Volume 108, pages 2131–2141, 2023

The crystal structure of feitknechtite (β-MnOOH) and a new MnOOH polymorph

Jeffrey E. Post[1,*], Peter J. Heaney[2], Eugene S. Ilton[3], and Evert J. Elzinga[4]

[1]Department of Mineral Sciences, Smithsonian Institution, P.O. Box 37012, Washington, DC 20013-7012, U.S.A.
[2]Department of Geosciences, Penn State University, University Park, Pennsylvania 16802, U.S.A.
[3]Pacific Northwest National Laboratory, 902 Battelle Boulevard, Richland, Washington 99352, U.S.A.
[4]Department of Earth & Environmental Sciences, Rutgers University, Newark, New Jersey 07102, U.S.A.

Abstract

Studies suggest that feitknechtite (β-MnOOH) is a prevalent, and perhaps necessary, intermediate phase during the synthesis of birnessite-like phases, the abiotic oxidation of Mn^{2+}, and the transformation of biogenic hexagonal phyllomanganates to more complex Mn oxides in laboratory and natural systems. Researchers have generally described feitknechtite as consisting of pyrochroite-like (or cadmium iodide-like) Mn-O octahedral layers, but a detailed crystal structure has not been reported. We used TEM/SAED and powder XRD and Rietveld refinements to derive the unit cell and, for the first time, report a complete structure description for feitknechtite (β-MnOOH). Rietveld refinements were also completed for three natural feitknechtite/hausmannite samples, and time-resolved synchrotron XRD experiments were used to follow the thermal transformation of feitknechtite to hausmannite. Additionally, we identified and report the structure for a second, and perhaps novel, MnOOH polymorph (proposed designation ε-MnOOH), mixed with the synthetic feitknechtite, that is similar to β-MnOOH but with a different layer stacking.

Keywords: Feitknechtite, manganese oxide, Beta-MnOOH, Rietveld, birnessite

Introduction

Feitknecht and Marti (1945) observed that oxidation of a suspension of synthetic $Mn(OH)_2$ resulted in a hydrated oxide of tri- and divalent Mn with a crystal structure related to that of hausmannite (Mn_3O_4). The hydrate was distinguished from hausmannite by the presence of a strong extra line (of unspecified *d*-spacing—only a line drawing was shown) in the low-angle region of the powder diffraction pattern. Frondel (1953) described a natural analog of this same hydrous Mn oxide as an alteration product of natural $Mn(OH)_2$ (pyrochroite) crystals from Sweden and Franklin, New Jersey. He called this new mineral hydrohausmannite, the same name proposed by Feitknecht and Marti (1945) for their synthetic material. Frondel (1953) also observed the same characteristic low-angle strong line noted by Feitknecht and Marti (1945) in the powder XRD pattern, and Frondel (1953) reported the *d*-spacing as 4.65 Å. Electron microscopy studies by Feitknecht et al. (1962), however, revealed that synthetic hydrohausmannite was actually a mixture of Mn_3O_4 (hausmannite) and a second phase that they called β-MnOOH. Bricker (1965) examined a hydrohausmannite sample from Sweden and confirmed that it, too, was a mixture of the same two phases. He proposed that β-MnOOH be given the mineral name feitknechtite and that hydrohausmannite be discredited.

Synthesis experiments by Bricker (1965) suggested that a series of compounds might exist spanning the composition range from $Mn(OH)_2$ to MnOOH. They observed that a mixture of β-MnOOH and hausmannite always formed from rapid oxidation of water suspensions of $Mn(OH)_2$, and that the solids transform to manganite (γ-MnOOH) upon standing. Hem (1978) and Hem et al. (1982) similarly report that β-MnOOH is the phase commonly obtained when Mn^{2+} is air-oxidized but that it is metastable and changes to manganite on aging in aerated solutions. They also suggested that it is an important intermediate for various Mn oxidation reactions, particularly in natural systems at temperatures <20 °C, where aqueous systems might first form feitknechtite as the precursor to MnO_2 phases, e.g., lake and ocean nodules. Klewicki and Morgan (1999) concluded that dissolution of MnOOH phases by Mn(III)-stabilizing ligands (e.g., citrate, EDTA, and pyrophosphate) at circumneutral pH conditions might be a significant factor in Mn cycling in natural waters.

Many researchers have suggested that Mn oxides in natural systems derive from biogenic oxidation of dissolved Mn^{2+} or by alteration of biogenic hexagonal birnessite-like phases to more crystalline secondary oxides. For example, Mandernack et al. (1995) observe that oxidation of aqueous Mn^{2+} by spores of *Bacillus* bacterium, strain SG-1, in HEPES-buffered water and seawater systems, pH 7.4–8.0, produces predominantly hausmannite and feitknechtite at high-Mn^{2+} concentrations (>~1 mM), whereas feitknechtite is favored at temperatures <~25 °C. Luo et al. (1998) report that feitknechtite is an intermediate phase initially formed during synthesis of birnessite-like material via oxidation of $Mn(OH)_2$ with permanganate and acetate. Bargar et al. (2005) demonstrate that biogenic hexagonal birnessite reacts with Mn^{2+} to form triclinic birnessite-like phases for [Mn^{2+}] <500 μM but forms feitknechtite at higher concentrations at near neutral pH. Elzinga (2011) and Lefkowitz et al. (2013) determined that dissolved Mn^{2+} converts hexagonal birnessite-like phases to feitknechtite and manganite at neutral pH and above, but that only feitknechtite forms at pH 7 to 8.5 for low-Mn^{2+} concentra-

* E-mail: postj@si.edu

0003-004X/23/0011–2131$05.00/DOI: https://doi.org/10.2138/am-2022-8729

tions (274 μM). Elzinga (2011) suggests that feitknechtite is the first mineral to form from the comproportionation reaction, $Mn^{2+} + Mn^{4+}O_2 + 2H_2O = 2Mn^{3+}OOH + 2H^+$, and he argues that feitknechtite is a necessary precursor to the more stable manganite. Lefkowitz et al. (2013) observe that feitknechtite also forms by autocatalytic oxidation of Mn^{2+} by O_2 in solution and by surface oxidation of Mn^{2+} by O_2 on goethite and hematite surfaces, and they conclude that feitknechtite is an important metastable Mn oxide phase in geochemical systems exhibiting abiotic Mn^{2+} oxidation. Moreover, β-MnOOH is commonly observed as an intermediate during the materials synthesis of Mn oxides, such as manganite nanowires (Portehault et al. 2010).

β-MnOOH (feitknechtite) is one of three naturally occurring MnOOH polymorphs, along with α-MnOOH (groutite) and γ-MnOOH (manganite). Yamamoto et al. (1981) report synthesis of a fourth polymorph, δ-MnOOH. Bricker (1965) infers that the structure of β-MnOOH is closely related to that of brucite-like pyrochroite [$Mn(OH)_2$], but with a decrease of the basal spacing from 4.72 to 4.62 Å as a consequence of the oxidation of Mn^{2+} to Mn^{3+}. Various researchers have described feitknechtite as consisting of pyrochroite-like (or cadmium iodide-like) Mn-O octahedral layers (Feitknecht et al. 1962; Bricker 1965; Meldau et al. 1973; Mandernack et al. 1995; Portehault et al. 2010; Grangeon et al. 2017), but a detailed crystal structure has not been reported. Bricker (1965) proposed a tetragonal unit cell with $a = 8.6$ Å and $c = 9.3$ Å, whereas Mandernack et al. (1995) and Portehault et al. (2010) report powder XRD patterns for feitknechtite that were similar to each other but different from that of Bricker (1965). Meldau et al. (1973) conclude that feitknechtite is an isotype of pyrochroite and propose a trigonal unit cell similar to that phase. Chukanov et al. (2021) also assume a trigonal unit cell with $a = 3.32$ Å and $c = 4.71$ Å. Based on selected area electron diffraction patterns and XRD data, Portehault et al. (2010) propose a monoclinic unit cell that is close to that determined for synthetic Na-birnessite by Post and Veblen (1990).

The studies above suggest that feitknechtite (β-MnOOH) is a prevalent, and perhaps necessary, intermediate phase to promote the precipitation of birnessite-like phases during the abiotic oxidation of Mn^{2+} and the transformation of biogenic hexagonal phyllomanganates to more complex Mn oxides in laboratory and natural systems. In light of this potentially critical role, a better understanding is required of the atomic structure of feitknechtite to model its chemical reactivity, thermodynamic stability, and phase transformation pathways. For the current study, we used TEM/SAED and powder XRD and Rietveld refinements to derive the unit cell and, for the first time, the detailed atomic structure for feitknechtite (β-MnOOH). We also present Rietveld refinements for three natural feitknechtite/hausmannite samples, and we describe the thermal transformation of feitknechtite to hausmannite based on temperature-resolved synchrotron XRD.

Samples and methods

Sample description

Synthetic samples of β-MnOOH were prepared by reacting a synthetic hexagonal birnessite-like phase with 274 μM Mn^{2+} solution at near-neutral pH (Elzinga (2011). In addition, we investigated three natural samples of feitknechtite and hausmannite after pyrochroite from the Wessels Mine, South Africa, Långban, Sweden (NMNH B7731), and Franklin, New Jersey (NMNH R2205).

Scanning electron microscopy (SEM)

Backscattered electron (BSE) imaging, using a GAD detector, and energy-dispersive spectrometry (EDS) X-ray analyses were carried out in the low-vacuum mode using a scanning electron microscope (FEI Nova NanoSEM 600; Department of Mineral Sciences, Smithsonian Institution) for powder samples of synthetic and natural feitknechtite dispersed onto a carbon substrate. EDS analyses were performed on uncoated samples using 15 keV accelerating voltage.

Fourier transform infrared spectroscopy (FTIR)

Samples were disaggregated under acetone in a mortar and pestle and sieved through a 325 mesh (<44 μm) sieve. Then, 0.5 mg of synthetic feitknechtite was milled with ~250 mg KBr using a SPECAC ball mixing mill for 1–2 min and pressed into a pellet. Transmission vibrational spectra were collected on a Nicolet 6700 Analytical FTIR Spectrometer for a range of 400 to 4000 cm^{-1}. The resolution was set at 3.86 cm^{-1}, and 64 scans were co-added for each spectrum. The background spectrum was collected using a KBr blank pellet. The Omnic 8 software (Nicolet) was used to view data during data collection.

Transmission electron microscopy (TEM)

Powdered samples of the synthetic and the South African feitknechtite were suspended in ethanol and dispersed onto holey carbon copper TEM grids. Selected area electron diffraction (SAED) and high-resolution transmission electron microscope (HRTEM) analyses were performed with a Philips 420 TEM and an FEI Talos F200X (S)TEM using acceleration voltages of 120 and 200 kV, respectively, at the Materials Characterization Laboratory, Penn State University. Simulations of selected area electron diffraction patterns were calculated using SingleCrystal software (CrystalMaker Software Ltd.).

X-ray photoelectron spectroscopy (XPS)

For XPS analysis, data collection and fitting procedures were followed as reported by Ilton et al. (2016). A powder sample of the synthetic feitknechtite was mounted on a strip of conductive copper tape affixed to a copper stub and then pressed with a clean borosilicate glass block. Measurements were conducted with a Kratos Axis Ultra DLD spectrometer with an Al*K*α X-ray source (1486.7 eV) operating at 10 mA and 15 kV. Magnetic immersion lenses were used to improve collection efficiency. The instrument work function was calibrated to give a binding energy (BE) of 83.96 ± 0.05 eV for the $4f_{7/2}$ line of metallic gold. The spectrometer dispersion was adjusted to yield a BE of 932.62 eV for the Cu2$p_{3/2}$ line of metallic copper. Measurements of the Mn2*p*, Mn3*s*, Mn3*p*, and O1*s*, lines were conducted with a step size of 0.1 eV, an analysis area of 300 × 700 μm, and pass energies (PE) of 20 or 40 eV. The resultant full-width at half maximum (FWHM) values for the Ag3$d_{5/2}$ line were 0.54 and 0.77 eV, respectively. The low sensitivity of the Mn3*s* line resulted in measurements only with PE = 40 eV. Survey scans were conducted at PE = 160 eV and step size = 0.5 eV. XPS spectra were fit by non-linear least squares after Shirley background subtractions with the CasaXPS curve resolution software package. Gaussian/Lorentzian contributions to line shapes were numerically convoluted with a Voigt function.

X-ray diffraction and Rietveld refinement

The samples used for X-ray diffraction were hand ground under acetone in an agate mortar and passed through a 325-mesh sieve and loaded into 0.7 mm quartz-glass or 1 mm (ID) polyimide (APS) capillaries. XRD data for the synthetic sample were collected: (1) at the advanced photon source (APS) GeoSoilEnviroCARS (GSECARS) 13-BM-C beamline, using 0.83154 Å radiation and a CCD detector, and (2) at the APS high-resolution XRD beamline 11BM, using a wavelength of 0.414211 Å. Conventional XRD data for the mineral samples were collected using a Rigaku DMAX-Rapid diffractometer (Smithsonian Institution) with a curved imaging plate, using Mo radiation. A LaB_6 powder (NIST SRM660a) was used to calibrate experimental instrument parameters. Preferred orientation of the powder was eliminated through a combination of specimen rotation, use of a capillary sample holder, and full intensity integration of the diffraction rings, as obtained using the program Dioptas (Prescher and Prakapenka 2015) (APS data) or 2DP (Rigaku) for the Mo radiation patterns, with a polarization factor of 0.99.

High-temperature XRD of β-MnOOH was performed at the APS 13-BM-C beamline with an X-ray wavelength of 0.83154 Å. Synthetic feitknechtite powder was loaded into a 0.7 mm thin-walled quartz capillary with one end unsealed to release water when heating. An electrically resistive forced air heater, using He as the transport gas, was placed directly below the capillary, and temperature was measured using a thermocouple, which was calibrated through phase transitions of

$RbNO_3$, yielding an estimated temperature error of ± 1.5 °C. Temperature-resolved data from 25 to 424 °C were collected as a series of 15 s exposures at 3 °C increments. During each exposure, the sample was rotated through a 75° angle.

Indexing of the powder X-ray diffraction peaks and Rietveld refinements (Rietveld 1969) was performed using the General Structure Analysis System-II (GSAS-II) software (Toby and Von Dreele 2013). Diffraction data generated by the LaB_6 standard (NIST SRM 660a) were used to calibrate peak profile parameters that described instrumental broadening. For all samples, diffraction peak profiles were fit with a pseudo-Voigt function as parameterized by Thompson et al. (1987), and microstrain anisotropic broadening terms by Stephens (1999).

Results

Structures of feitknechtite and MnOOH-Phase 2

The high-resolution powder diffraction data (APS 11BM) were indexed by a monoclinic *C*2/*m* unit cell with parameters given in Table 1. This unit cell successfully indexed all observed diffraction peaks, except for several weak peaks (strongest <~2.5% of the most intense feitknechtite peak), e.g., at 2.82, 2.55, 2.24, and 1.71 Å. Using GSASII, we were able to index the extra weak reflections separately using a unit cell for which *a* and *b* were similar to those of feitknechtite, but with a β angle close to 90° and *c* of ~4.60 Å (Table 1). Bricker (1965) reported that his attempts to synthesize β-MnOOH from aqueous solution under various conditions always produced mixtures of Mn oxide phases, with impurities such as hausmannite and other unidentified MnII/MnIII oxides. XRD patterns of the natural specimens from South Africa, Franklin, and Sweden did not show the extra peaks for the impurity phase observed in our synthetic sample. The unit-cell parameters determined for feitknechtite are close to those measured from our TEM SAED patterns and to those determined from SAED patterns from synthetic β-MnOOH by Portehault et al. (2010).

Based on the similarity of the feitknechtite unit-cell parameters to those of Na-birnessite (Table 1), we selected initial Mn and O atom positions for the Rietveld refinement that were similar to those in monoclinic Na-birnessite, as reported by Post and Veblen (1990), but adjusted for the shorter *c* axis. Only background parameters, scale factor, unit-cell parameters, and peak profile coefficients were varied in the initial refinement cycles; background intensities were fitted with a Chebyshev function using 5–7 terms. The overall good fit to the observed pattern confirmed that the basic structure model was correct.

The final refinement stages for the synthetic feitknechtite sample also included the impurity phase, "MnOOH-Phase 2," using the unit cell determined by the indexing program. As the unit cell indicated a layer structure similar to that of feitknechtite, but with a different β angle, the same Mn and O positions as determined for feitknechtite were applied to the starting structure model for Phase 2. Phase 2 fit the extra peaks well, and the R_{wp} goodness-of-fit parameter improved from 0.175 to 0.117. The refinement for the synthetic mixture yielded abundances of ~86 wt% feitknechtite and ~14 wt% Phase 2. After convergence, the O atom positions for feitknechtite and Phase 2 were refined. Refinements of the feitknechtite Mn and O occupancy factors yielded values that were not significantly different than 1.0 and were fixed at unity.

The final refinement parameters and other structure details for RT synthetic feitknechtite (β-MnOOH) and MnOOH-Phase 2, using the APS 11BM data, are given in the Online Materials CIF[1], and atom positions and selected bond distances are reported in Table 2. The final observed, calculated, and difference X-ray diffraction patterns are plotted in Figure 1, and modeled and observed SAED patterns for multiple zone axes are shown in Figure 2. Polyhedral structure representations are shown in Figure 3.

Table 1. Rietveld refined unit-cell parameters (*C*2/*m*) for β-MnOOH (feitknechtite) and MnOOH-Phase2, and synthetic Na-birnessite ($P\bar{1}$)

Sample	*a* (Å)	*b* (Å)	*c* (Å)	α (°)	β (°)	γ (°)
β-MnOOH	5.6541(4)	2.89075(2)	4.8347(3)		108.0709(1)	
Impurity phase	5.6509(1)	2.89072(4)	4.6025(1)		89.976(6)	
South Africa	5.523(1)	2.901(1)	4.866(1)		108.44(1)	
Sweden	5.501(1)	2.902(1)	4.847(1)		108.58(1)	
Franklin, New Jersey	5.382(1)	2.934(1)	4.886(1)		108.86(1)	
Na-birnessite[a]	5.1746(2)	2.8474(1)	7.3319(4)	89.444(5)	103.181(4)	89.948(6)

[a] Post et al. (2002).

Table 2. Atomic coordinates and selected bond distances (Å) for β-MnOOH (feitknechtite) and MnOOH-Phase 2

Feitknechtite

Atom	*x*	*y*	*z*	Site occupancy factor	U_{iso}
Mn	0	0	0	1.0	0.0066(2)
O	0.4206(2)	0	0.2217(2)	1.0	0.00227(2)
Mn-O	2.2856(8) (×2)				
	1.9333(6) (×4)				
<Mn-O>	2.05				
O-O	2.800(2) (×2)				
O-O	2.568(2)				
O-O	2.559(2)				

MnOOH-Phase 2

Atom	*x*	*y*	*z*	Site occupancy factor	U_{iso}[a]
Mn	0	0	0	1.0	0.005
O	0.3579(6)	0	0.191(1)	1.0	0.005
Mn-O	2.206(4) (×2)				
	1.872(3) (×4)				
<Mn-O>	1.98				
O-O	2.891 (×2)				
O-O	2.380(8)				
O-O	2.583(8) (×2)				

Notes: e.s.d. values are those reported from the Rietveld refinement, and previous studies indicate might be underestimated by an order of magnitude, or more (Post and Bish 1989).

[a] Temperature factors were held fixed to values given.

The structure model determined above was successfully applied to the mineral samples from South Africa, Sweden, and New Jersey. The unit-cell parameters are listed in Table 1. It was also used for Rietveld refinements during the heating of the synthetic powders from RT to 424 °C. When present, the hausmannite phase was fit using starting structure parameters reported by Baron et al. (1998).

Discussion

Comparison of the feitknechtite (β-MnOOH) structure with that of related Mn hydroxides

As discussed above, because feitknechtite is readily formed by the oxidation of pyrochroite, many researchers have assumed that its structure is some permutation of the pyrochroite brucite-like structure (Aminoff 1919). A detailed structure description, however, that includes unit-cell parameters and atom positions, has not previously been reported. Our structure solution and refinement confirm that feitknechtite is constructed of parallel lay-

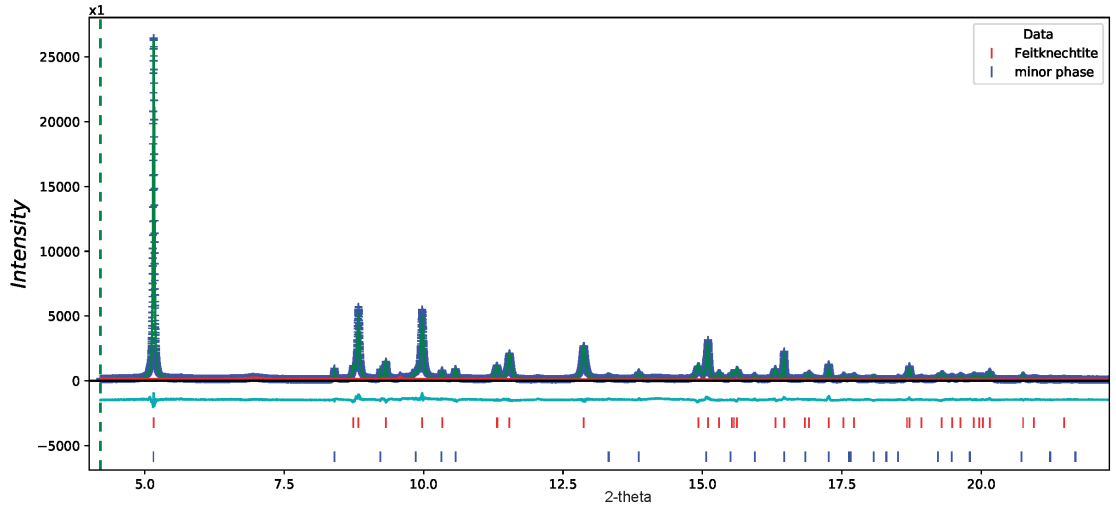

Figure 1. Final Rietveld observed (blue crosses), calculated (solid green) and difference (light blue) powder diffraction patterns for β-MnOOH and phase 2 MnOOH. The vertical marker lines indicate positions for the indexed peaks, and the refined background is shown as the solid red line. λ = 0.414211 Å. (Color online.)

ers of Mn^{3+}-(O,OH) octahedra, making it the only known purely Mn^{3+} layer structure. The Mn^{3+} Jahn-Teller distortions for the Mn-(O,OH) octahedra result in elongated axial bonds [2.286(1) Å] relative to the four equatorial distances [1.933(1) Å], similar to those observed in other Mn^{3+} oxides, e.g., 2.28 and 1.93 Å, respectively, in hausmannite (Jarosch 1987). The calculated mean Mn-O bond length of 2.05 matches well the values of 2.04 and 2.05 Å reported for <Mn-O> bond distances in manganite (γ-MnOOH) and groutite (α-MnOOH), respectively, (Kohler et al. 1997) and of 2.05 Å for hausmannite (Baron et al. 1998). This

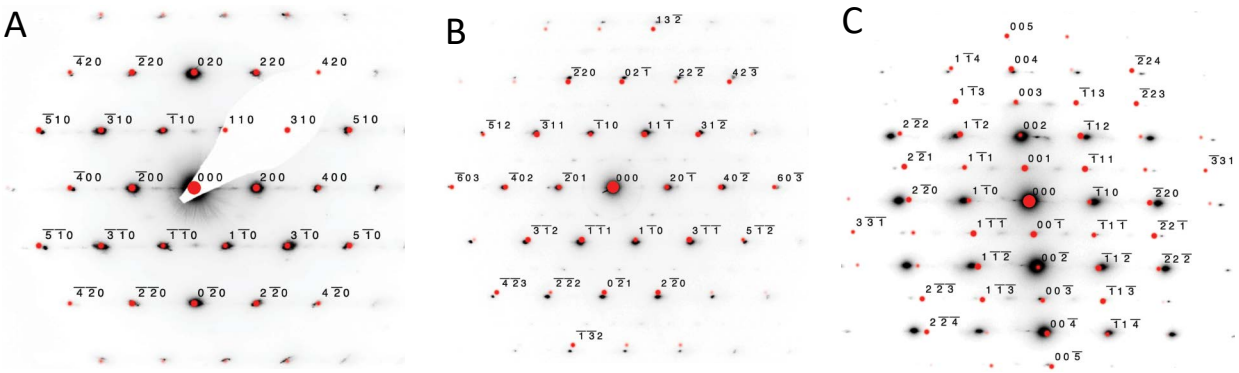

Figure 2. Observed (black) and modeled (red) selected area electron diffraction patterns for synthetic β-MnOOH along the following zone axes: (**a**) [001]; (**b**) [112]; and (**c**) [110]. (Color online.)

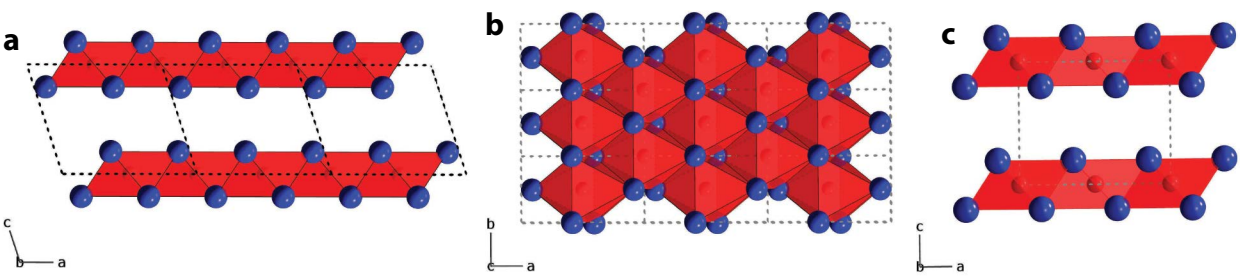

Figure 3. Polyhedral drawing of the β-MnOOH (feitknechtite) structure looking (**a**) along *b*, and (**b**) along *c*, and (**c**) for MnOOH-Phase 2 along *b*. The Mn^{3+}-O octahedra are shown in red, and the O/OH positions are plotted as blue spheres. The unit-cells are indicated by dashed lines. (Color online.)

observation is consistent with our XPS data (below) showing that, within error, all Mn in our synthetic feitknechtite is trivalent. The pronounced Jahn-Teller octahedral distortions reduce the structure symmetry from trigonal in pyrochroite (space group $P\bar{3}m$) to monoclinic (space group $C2/m$).

Energy-dispersive spectroscopy revealed only Mn and O in the synthetic sample. Charge balance for the chemical formula MnOOH requires that half of the O atoms are OH^- anions, as in the MnOOH polymorphs groutite and manganite, and indicated by FTIR (below). Single-crystal refinements for groutite and manganite (Kohler et al. 1997) revealed a disparity in the Mn-O and Mn-OH bond lengths, with Mn-OH longer for both axial and equatorial octahedral distances. Oxygen and OH groups are disordered over the one symmetrically unique O atom site in feitknechtite, and, therefore, cannot be distinguished. The O atoms at the base of an octahedral sheet in feitknechtite are situated in nearly vertical alignment above the O atoms at the top of the octahedral sheet below (Fig. 3). The O-O distance across the interlayer in feitknechtite is 2.80 Å, which is typical for OH-O hydrogen bonds (Baur 1972). This relationship suggests that the H atoms are arranged such that OH at the base of one octahedral sheet will lie above O atoms at the top of the adjacent sheet below. Consequently, some H atoms within an interlayer will be closer to one sheet and some closer to the other in a disordered fashion. This network of H-bonds across the interlayer binds the octahedral sheets tightly together, resulting in a closer layer spacing of 4.62 Å in feitknechtite, as compared to 4.72 Å in $Mn(OH)_2$-pyrochroite (Bricker 1965)]. In groutite, the O1···H2-O2 distance across the short dimension of the 1×2 octahedral tunnels is 2.57 Å, accounting for its slightly smaller "layer spacing" (distance between parallel double chains) of 4.557 Å (Kohler et al. 1997).

The feitknechtite FTIR spectrum shows OH-related modes similar to those observed for manganite (Fig. 4). Kohler et al. (1997) interpret the broad peak at about 2500–2700 cm^{-1} for manganite as arising from OH stretching modes associated with observed H-bonds of ~2.6 Å and assigned the peaks between ~900 and 1200 cm^{-1} to OH bending modes. The OH stretch peak for feitknechtite is shifted to a higher frequency (2750 cm^{-1}) relative to that in manganite (2650 cm^{-1}), indicating a longer average H-bond (Novak 1974), consistent with our observed value of ~2.80 Å.

Our refined occupancies for Mn did not reveal significant vacancy concentrations, although, as discussed below, minor vacancies may give rise to possible superstructures. In the Rietveld refinements, the Mn occupancy factor was strongly correlated with the overall scale factor, making the accurate determination of the Mn occupancy difficult. We have observed similar challenges when trying to determine vacancy concentrations for Mn sites in other Mn oxide layer structures, e.g., birnessite-like phases (unpublished results). Difference Fourier maps calculated during the Rietveld refinements did not show any areas of electron density in the region between the layers that might have corresponded to cations above and below possible octahedral Mn vacancies. Model calculations showed that the refinement is sensitive to the presence of such interlayer cations.

The X-ray diffraction patterns showed that all the natural

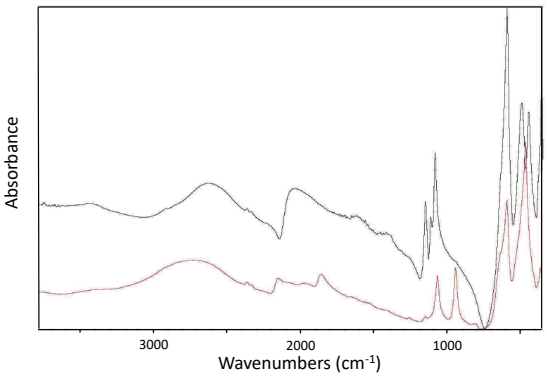

Figure 4. FTIR spectra for synthetic feitknechtite (lower) and manganite (upper). (Color online.)

"feitknechtite" samples included some hausmannite, and Rietveld refinements yielded 50, 30, and 10 wt% hausmannite in the South Africa, Sweden, and Franklin, New Jersey, samples, respectively. Selected area electron diffraction of the South African material suggested that the intergrowth of feitknechtite and hausmannite was topotaxial (Figs. 5a and 5b), with a shared orientation of the 020 planes of hausmannite (d_{020} = 2.879 Å) and the $1\bar{1}0$ planes of feitknechtite ($d_{1\bar{1}0}$ = 2.538 Å). The refined structures for natural feitknechtite samples did not significantly differ from each other or from that of the synthetic sample. The unit-cell parameters showed some slight variation among the natural samples (Table 1), particularly in the *a* and *b* dimensions, especially for the Franklin sample.

MnOOH-Phase 2 (ε-MnOOH)

Portehault et al. (2010) derived the same unit-cell parameters as we did for feitknechtite, but they observed that their unit cell "cannot account satisfactorily for feitknechtite because unindexed reflections are still present (e.g., 29.7 and 30.8° on the XRD pattern)." As they used Cu*K*α radiation (λ = 1.5418 Å), those peaks correspond to *d*-spacings of 3.008 and 2.903 Å. As described above, we also detected additional peaks in our powder XRD data, albeit in different positions, and we attribute those peaks to a secondary MnOOH phase with a similar unit cell to that of feitknechtite, but with β close to 90° instead of 108.07°. Rietveld analysis indicated that the synthetic feitknechtite contained ~14 wt% of this "MnOOH-Phase 2." Although the closeness in the structures of β-MnOOH and Phase 2 made it difficult to distinguish the two phases by TEM, selected area electron diffraction did reveal a doubling of diffraction spots for both the synthetic and the South African material, indicating epitaxial intergrowths of phases with slightly disparate unit-cell parameters (Fig. 5c). The refinement results in Table 2 and the structure drawing in Figure 3 show that this Phase 2 octahedral Mn^{3+}-O layer structure is nearly identical to that of feitknechtite, but adjacent layers are stacked directly above each other, as in pyrochroite, without an offset along *a* (Fig. 6). The calculated Mn-O bond distances revealed a strong Jahn-Teller type distortion, confirming that the Mn is predominantly trivalent, but the mean Mn-O distance of 1.98 Å is shorter than the value for <Mn-O> of 2.05 Å observed in feitknechtite. Nevertheless, the

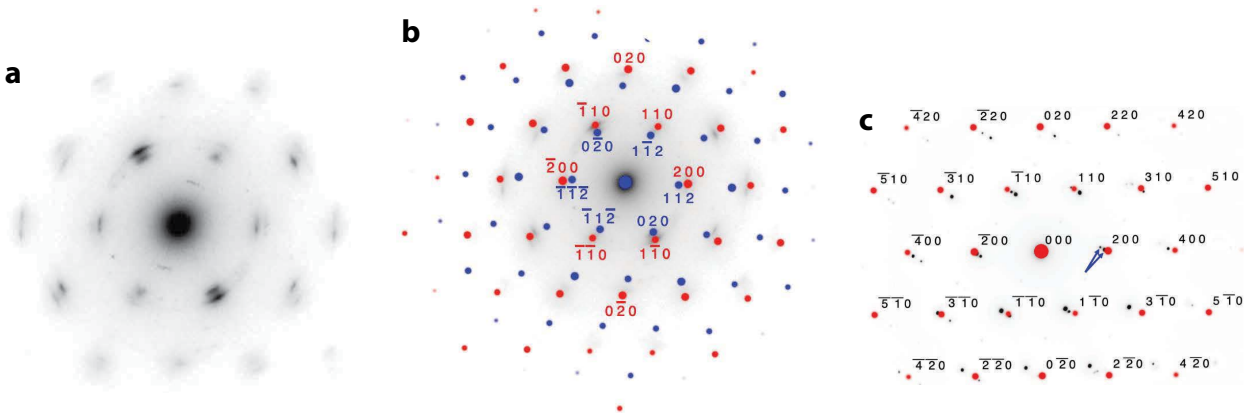

Figure 5. (**a**) Unlabeled SAED pattern for South African sample showing doubled spots indicative of topotaxial intergrowth of feitknechtite and hausmannite. (**b**) Simulated SAED patterns for feitknechtite along ZA [001] (red) and for hausmannite along ZA [$\bar{2}$01] (blue), superimposed on the above pattern. (**c**) SAED pattern for synthetic β-MnOOH (ZA [001]) revealing a slight doubling of diffraction spots (arrowed), suggestive of the intergrowth of feitknechtite and Phase-2. (Color online.)

ratio of the axial-to-equatorial octahedral Mn-O bond lengths was 1.18 for both phases. The difference in mean bond lengths might not be significant as the small fraction of Phase 2 in the sample challenged the determination of accurate atom positions. If the shorter mean Mn-O bond distance in Phase 2 was correct, however, it might indicate the presence of some Mn^{4+} in the octahedral site, with charge balance maintained by the replacement of some OH^- by O^{2-}. As the synthetic feitknechtite was formed by reacting hexagonal birnessite (predominantly Mn^{4+}) with aqueous Mn^{2+}, it is possible that Phase 2 represents an intermediate, or second, phase with some remnant Mn^{4+}. To our knowledge, Phase 2 is a previously unreported polymorph of MnOOH, and we propose the designation ε-MnOOH (epsilon-MnOOH) to distinguish it from other reported MnOOH polymorphs.

The octahedral sheet stacking relationship between feitknechtite and ε-MnOOH is approximately the same as that between triclinic and hexagonal birnessite structures (Fig. 7). In hexagonal birnessite, octahedral (Mn^{4+},Mn^{3+})-O sheets, with predominantly Mn^{4+}, stack vertically to yield a structure with $P\bar{3}$ symmetry, which can also be described as an orthohexagonal $C2/m$ unit cell with β = 90°. The unit cell for ε-MnOOH is similar to the orthohexagonal cell; β is near 90°, but the a/b ratio is 1.96, resulting from the Jahn-Teller distorted Mn^{3+} octahedra, compared with 1.73 in trigonal birnessite. The octahedral sites in the structure of triclinic Na-birnessite, with formula $Na_{0.58}Mn_2O_4 \cdot 1.7H_2O$ (Post and Veblen 1990), contain ~2/3 Mn^{4+} and 1/3 Mn^{3+}. Adjacent octahedral sheets are offset along a, as in feitknechtite, and the β angle for Na-birnessite in the pseudo-$C2/m$ unit cell is ~103° (Post et al. 2002).

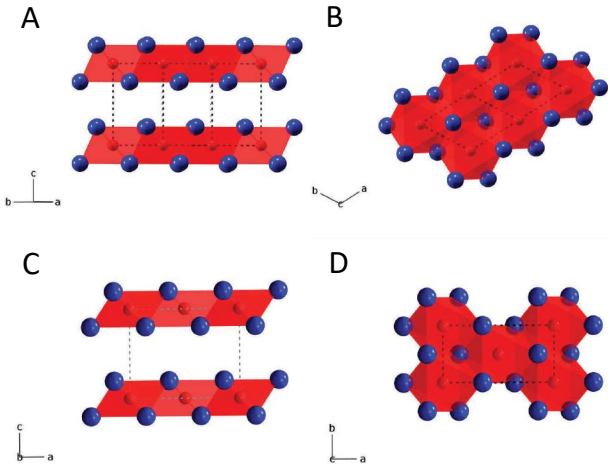

Figure 6. Polyhedral structure representation of MnOOH-Phase 2 (**a** and **b**) and pyrochroite (**c** and **d**), projected parallel and normal to the octahedral layers. The Mn-O octahedra are shown in red, and the O,OH atoms are dark blue spheres. (Color online.)

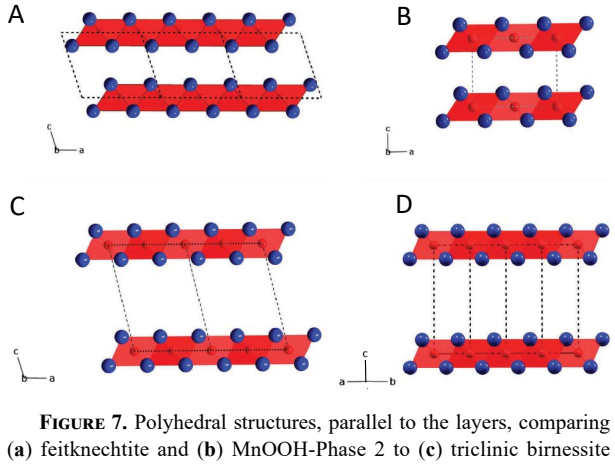

Figure 7. Polyhedral structures, parallel to the layers, comparing (**a**) feitknechtite and (**b**) MnOOH-Phase 2 to (**c**) triclinic birnessite (interlayer cations and water molecules omitted) and (**d**) hexagonal birnessite (interlayer cations and water molecules omitted). The Mn-O octahedra are shown in red, and the O,OH atoms are dark blue spheres. (Color online.)

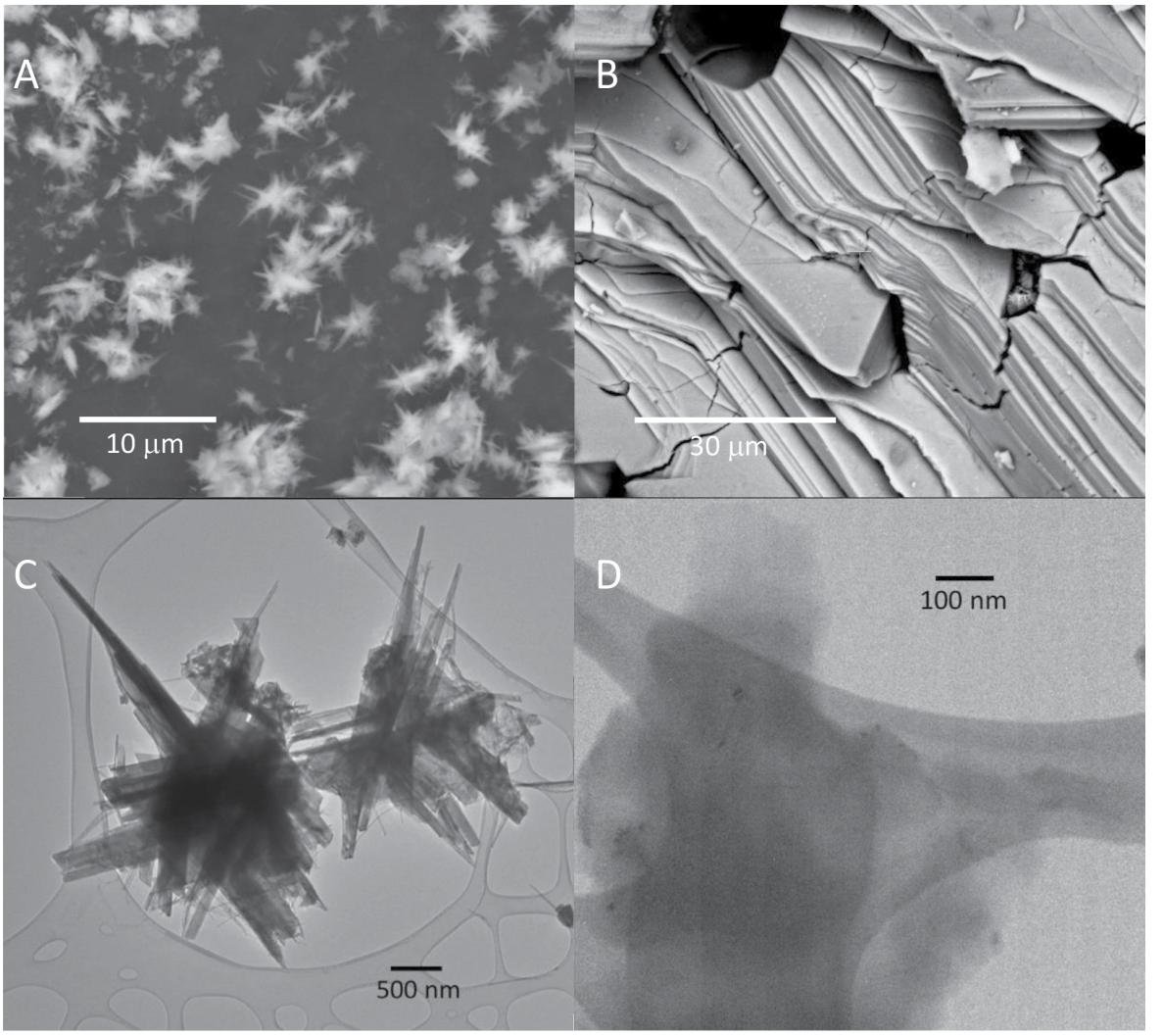

Figure 8. (**a**) SEM BSE image of β-MnOOH, (**b**) SEM BSE image of feitknechtite from South Africa, (**c**) TEM image of synthetic β-MnOOH, and (**d**) TEM image of feitknechtite from South Africa.

TEM and SEM analyses of feitknechtite microstructures

The SEM BSE and TEM images of the synthetic feitknechtite sample revealed clusters of ~0.3 × 0.5 μm lath-like crystals, oriented at ~120 ° to each other (Fig. 8). Energy-dispersive X-ray analysis showed the presence only of Mn and O. Portehault et al. (2010) observed similarly oriented crystal clusters in TEM images of synthetic feitknechtite and proposed that they were twinned crystals formed by the lateral assembly of primary nanorods.

The natural samples in the present study appeared fine-grained, with individual crystallites smaller than 0.5 μm, and with a layered texture (Fig. 9), likely pseudomorphed after the original pyrochroite. EDS analyses for these samples showed Mg in addition to Mn and O, and Zn for the Franklin sample. The average cation ratios were $Mn_{0.97}Mg_{0.03}$, $Mn_{0.93}Mg_{0.07}$, and $Mn_{0.87}Mg_{0.10}Zn_{0.03}$ for the samples from South Africa, Sweden, and Franklin, New Jersey, respectively. The Shannon (1976) ionic radii for Mg^{2+} of 0.86 Å, and for Zn^{2+} of 0.88 Å, are between those of Mn^{2+} (0.97 Å) and Mn^{3+} (0.785 Å), and therefore, might comfortably substitute for Mn in pyrochroite or feitknechtite, or hausmannite, which is associated with feitknechtite in all the natural samples. Luo et al. (1996) synthesized β-MnOOH with Mg as ~25% of the total cations.

Because the hausmannite was finely intermixed with the feitknechtite, it was not possible to determine whether the Mg and Zn were equally distributed between the two phases or more concentrated in one. Analyses from multiple sites on each sample showed general chemical homogeneity within a given sample. Mg and Zn are not Jahn-Teller cations; therefore, as they replace some of the Mn^{3+} in feitknechtite, the average Mn octahedral distortion will be reduced, with a consequent change in the ratio of the *a* and *b* unit-cell parameters. The Mn^{3+} octahedral distortion is elongated primarily along *a* (Fig. 2b), and therefore, one might expect that parameter and the *a*/*b* ratio should decrease with the addition of Mg or Zn. In fact, the observed *a*/*b* ratios follow that trend, with *a*/*b* values of 1.956 for synthetic feitknechtite, which

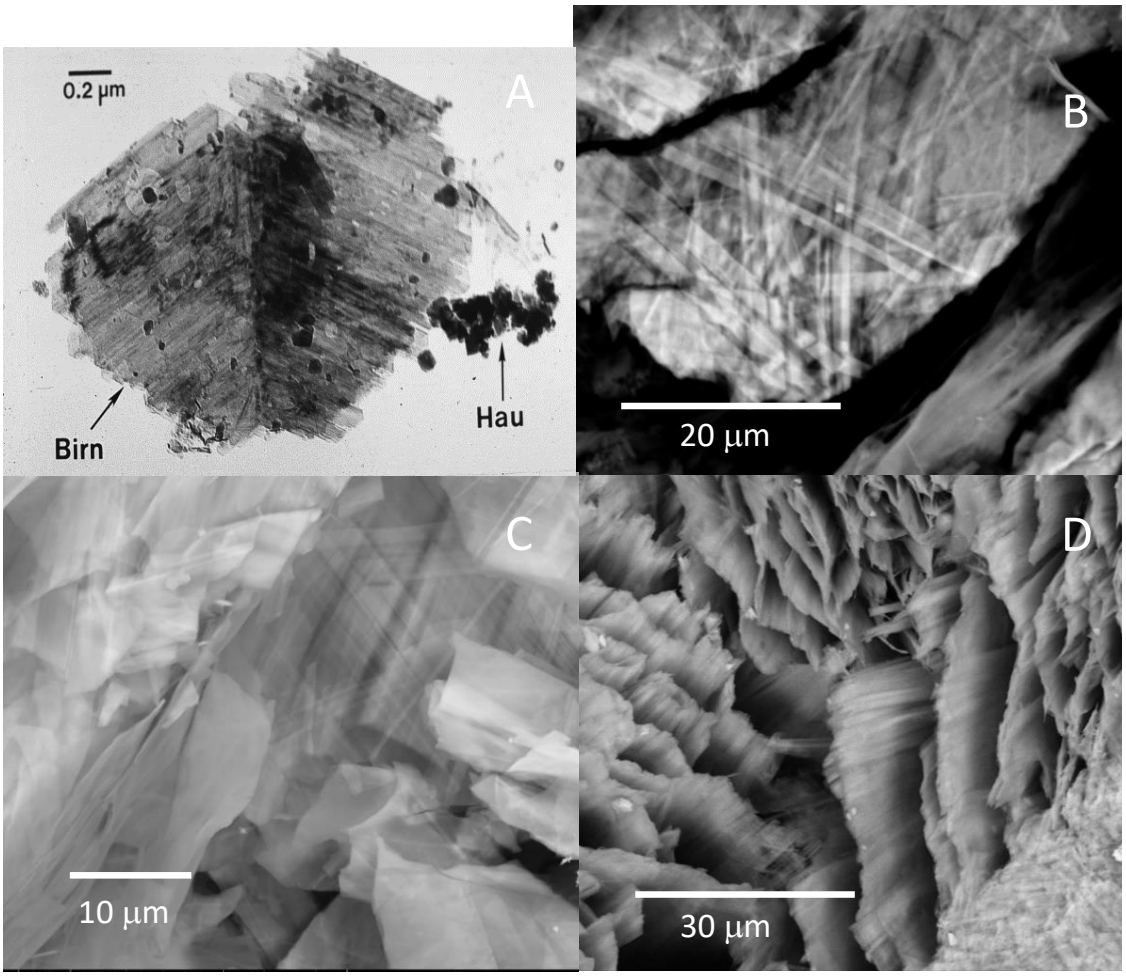

Figure 9. (**a**) TEM image of synthetic Na-birnessite (Post and Veblen 1990), (**b**) SEM BSE image of ranciéite from Alsace, France, (**c** and **d**) SEM BSE images of ranciéite from Spain.

has no Mg or Zn, 1.903 and 1.896, for the Swedish and South African samples with 0.07 and 0.03 Mg per octahedral cation site, respectively, and 1.834 for the Franklin sample with 0.1 Mg and 0.03 Zn per Mn site. It is also possible that the natural samples might have some Mn^{2+}, but with the admixed hausmannite, it is not clear how one might confirm its presence in feitknechtite.

The synthetic feitknechtite used in the current study was formed by reacting synthetic hexagonal birnessite, with predominantly Mn^{4+}-octahedral sheets, with aqueous Mn^{2+} solutions. The reduction of Mn^{4+} to Mn^{3+} triggers the transformation from birnessite to feitknechtite. As seen in Figure 10, the resulting lath-like feitknechtite crystals were elongated along b^*, normal to the direction of the axial Mn-O bonds in the Jahn-Teller distorted Mn^{3+} octahedra, which are parallel to the monoclinic a axis. Preferential growth in the direction of the shorter and stronger equatorial bonds is consistent with periodic bond chain theory (Hartman and Perdok 1955). On the other hand, superperiodicities and lattice disorder are concentrated along a*, likely as the result of localized intergrowths of Phase 2 with feitknechtite. The observed morphology suggests that the hexagonal birnessite crystals templated the growth of the feitknechtite crystals. Because of the trigonal symmetry of the Mn^{4+}-O octahedral sheet in the original birnessite, the newly formed feitknechtite crystals oriented and grew with equal probability in any of three directions at 120° to each other.

Feitknecht and Marti (1945) and Bricker (1965) synthesized feitknechtite by oxidation of $Mn(OH)_2$ (pyrochroite). Hem (1981) presumes that the similarity of the layer structures of feitknechtite and pyrochroite promotes the transformation from $Mn(OH)_2$ to β-MnOOH. In fact, the natural feitknechtite investigated in the present study formed, with hausmannite, as alterations of pyrochroite, retaining the crystal morphology of the original phase. X-ray diffraction patterns from many of these pseudomorphs show single-crystal spots rather than powder rings, consistent with a transformation that preserved the basic crystal structure.

Luo et al. (1998) determined that β-MnOOH is the intermediate phase when $Mn(OH)_2$ is oxidized by dissolved permanganate during the synthesis of birnessite-like phases. We have similarly observed that oxidation of $Mn(OH)_2$ in solution by O_2 initially forms β-MnOOH, which then transforms into a triclinic birnes-

site phase (unpublished results). As with the case of hexagonal birnessite, the trigonal symmetry of the pyrochroite Mn^{2+}/O octahedral sheets allows monoclinic β-MnOOH crystals to grow equally well in three orientations. TEM and SEM images of synthetic triclinic birnessite crystals (Fig. 9) commonly show sheets constructed of parallel lath-like components, sometimes twinned at 120° angles, which likely reflect the morphologies of the precursor monoclinic β-MnOOH crystals. Similarly, SEM images of the Ca-birnessite-like mineral ranciéite (Fig. 9) typically reveal sheet-like crystals that are composites of twinned lath-like components, despite their overall trigonal ($P\bar{3}$) symmetry (Post et al. 2008). Ranciéite is most typically found in the oxidation zones of Mn-rich deposits or in low-temperature mineralized veins and vugs in limestone (Ertl et al. 2005). It seems reasonable that the twinned, lath-like crystal morphology reflects pseudomorphic alteration from feitknechtite, which in turn transformed from pyrochroite.

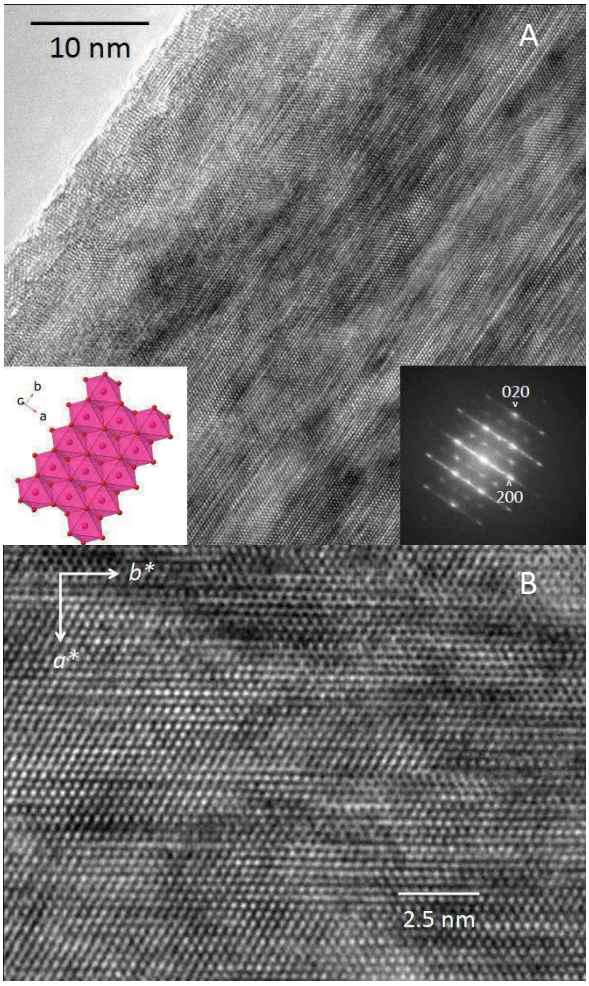

Figure 10. (**a**) HRTEM image of β-MnOOH lath with fast Fourier transform (inset) reveals that crystals are elongate along the *b** direction, with local superperiodicities and lattice disorder along the *a** direction. (**b**) Higher magnification HRTEM image reveals significant disorder along *a**, the direction of elongated Mn^{3+}-O bonds due to Jahn-Teller distortions. (Color online.)

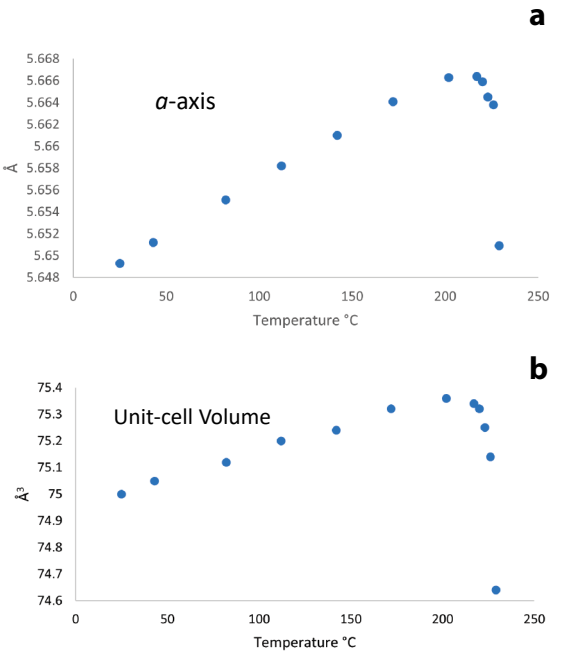

Figure 11. Temperature dependence of *a* (**a**) and unit-cell volume (**b**) for β-MnOOH. (Color online.)

Thermal transformation of β-MnOOH (feitknechtite) to hausmannite

When synthetic β-MnOOH was heated from 25 to ~200 °C, the structure showed a small but continuous thermal expansion (Fig. 11), with an increase in the unit-cell volume of 0.5%. The dependence of the unit-cell parameters on temperature (Fig. 11) reveals that most of the expansion occurred along the *a* direction (+0.3%), which is the direction of the longer axial Mn^{3+}-O octahedral bonds. Over this temperature range, the changes in the individual *b*, *c*, and β unit-cell parameters were 0.1% or less. Between ~200 and 230 °C, the transformation of feitknechtite to hausmannite was marked by a decrease in unit-cell volume by ~1%, mostly caused by ~0.3% contractions in the *a* and *b* parameters. Hausmannite was first detected in the diffraction pattern at 226 °C, and feitknechtite was absent by 244 °C. The Rietveld refinement for the diffraction pattern collected at 235 °C determined the sample was 82% hausmannite and 18% feitknechtite. Our results are consistent with TGA measurements (Yan et al. 2014), which showed an abrupt weight loss for β-MnOOH at ~225 °C. The X-ray diffraction data revealed no evidence for an intermediate amorphous phase. The transformation of feitknechtite to hausmannite requires loss of OH (as H_2O) and reduction of 1/3 of the Mn^{3+} to Mn^{2+}, according to the reaction:

$$3Mn^{3+}OOH \rightarrow Mn_2^{3+}Mn^{2+}O_4 + 3/2H_2O + ¼O_2. \quad (1)$$

The displacement of some of the Mn^{3+} and all of the newly reduced Mn^{2+} from the feitknechtite octahedral sheets to the interlayer region builds the hausmannite spinel structure (Fig. 12). Bricker (1965) concludes that hausmannite is a more stable phase than feitknechtite, but only slightly so. Interestingly, the reported transformation temperature for the dehydration of FeOOH (goe-

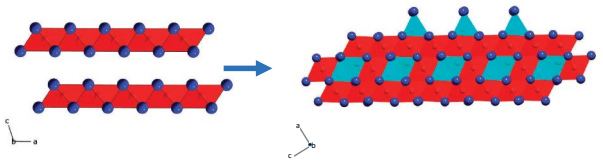

Figure 12. Polyhedral structural representation of transformation of β-MnOOH (left) to hausmannite (right) above ~225 °C. The Mn^{3+}-O octahedra are shown in red, the Mn^{2+}-O tetrahedra in light blue, and the O,OH (β-MnOOH) and O (hausmannite) atoms as dark blue spheres. (Color online.)

thite) to Fe_2O_3 (hematite) also is in the range of 240–255 °C (Özdemir and Dunlop 2000). In both cases, the trigger for the transformation is the loss of OH, accompanied by the reduction of some Mn in feitknechtite.

Implications

This study provides the first complete structure description for β-MnOOH (feitknechtite). Additionally, we identified and reported the structure for a second MnOOH phase (ε-MnOOH), similar to β-MnOOH but with a different layer stacking, and as such, it seems to be a new MnOOH polymorph. Several researchers have described feitknechtite as a requisite intermediate phase during the synthesis of technologically important Mn (hydr) oxides. It is also assumed to play a critical role in abiotic and biotic processes that produce and alter Mn oxide phases in various natural environments. The lack of knowledge of the atomic structure of feitknechtite has limited our understanding of its precise role and behavior in synthetic and natural redox reactions in manganiferous systems. Our work provides the formal structure description required for model calculations that will provide a better understanding of this phase and make possible predictions about the behavior of β-MnOOH (feitknechtite) under a range of conditions. It also provides an essential starting point for analyzing powder diffraction data to determine and monitor unit-cell parameters and other structure details and for quantitative phase analyses of Mn oxide samples that contain feitknechtite. Feitknechtite has been part of the Mn oxide conversation for more than seven decades, and it is satisfying to finally know what it is.

Acknowledgments

We thank Ke Wang of the Penn State Materials Characterization Laboratory for his assistance with the TEM analyses, and Joanne Stubbs and Peter Eng for their invaluable help with synchrotron data collection at the APS. E.S.I. was supported by the U.S. Department of Energy (DOE), Office of Science, Office of Basic Energy Sciences, Chemical Sciences, Geosciences, and Biosciences Division through its Geosciences Program at the Pacific Northwest National Laboratory.

Funding

Funding for this research was provided by National Science Foundation Grant EAR-1925903. Synchrotron XRD was performed at GSECARS (University of Chicago) Beamline 13-BM-C at the APS. GSECARS is supported by NSF EAR-1634415 and DOE GeoSciences DE-FG02-94ER14466. The Advanced Photon Source is operated under DOE Contract No. DE-AC02-06CH11357.

References cited

Aminoff, G. (1919) Über die Krystallstruktur des Pyrochroits. Geologiska Föreningens i Stockholm Förhandlingar, 41, 407–431, https://doi.org/10.1080/11035891909447000.

Bargar, J.R., Tebo, B.M., Bergmann, U., Webb, S.M., Glatzel, P., Chiu, V.Q., and Villalobos, M. (2005) Biotic and abiotic products of Mn(II) oxidation by spores of the marine Bacillus sp. strain SG-1. American Mineralogist, 90, 143–154, https://doi.org/10.2138/am.2005.1557.

Baron, V., Gutzmer, J., Rundlöf, H., and Tellgren, R. (1998) The influence of iron substitution on the magnetic properties of hausmannite, $Mn^{2+}(Fe,Mn)^{3+}O_4$. American Mineralogist, 83, 786–793, https://doi.org/10.2138/am-1998-7-810.

Baur, W.H. (1972) Prediction of hydrogen bonds and hydrogen atom positions in crystalline solids. Acta Crystallographica, B28, 1456–1465, https://doi.org/10.1107/S0567740872004455.

Bricker, O. (1965) Some stability relations in the system $Mn-O_2-H_2O$ at 25° and one atmosphere total pressure. American Mineralogist, 50, 1296–1354.

Chukanov, N.V., Varlamov, D.A., Pekov, I.V., Zubkova, N.V., Kasatkin, A.V., and Britvin, S.N. (2021) Coupled substitutions in natural MnO(OH) polymorphs: infrared spectroscopic investigation infrared spectroscopic investigation. Minerals, 11, 969–981.

Elzinga, E.J. (2011) Reductive transformation of birnessite by aqueous Mn(II). Environmental Science & Technology, 45, 6366–6372, https://doi.org/10.1021/es2013038. PubMed

Ertl, A., Pertlik, F., Prem, M., Post, J.E., Kim, S.J., Brandstätter, F., and Alfschuster, R. (2005) Ranciéite Crystals from Friesach, Carinthia, Austria. European Journal of Mineralogy, 17, 163–172, https://doi.org/10.1127/0935-1221/2005/0017-0163.

Feitknecht, V.W. and Marti, W. (1945) Über die Oxydation von Mangan(II)-hydroxyd mit molekularem Sauerstoff. Helvetica Chimica Acta, 28, 129–148, https://doi.org/10.1002/hlca.19450280113.

Feitknecht, V.W., Brunner, P., and Oswaldw, H.R. (1962) Über den einfluß der feuchtigkeit auf die oxydation von manganhydroxid durch molekularen sauerstoff. Zeitschrift für Anorganische und Allgemeine Chemie, 316, 154–160, https://doi.org/10.1002/zaac.19623160307.

Frondel, C. (1953) New manganese oxides: Hydrohausmannite and woodruffite. American Mineralogist, 38, 761–769.

Grangeon, S., Warmont, F., Tournassat, C., Lanson, B., Lanson, M., Elkaïm, E., and Claret, F. (2017) Nucleation and growth of feitknechtite from nanocrystalline vernadite precursor. European Journal of Mineralogy, 29, 767–776, https://doi.org/10.1127/ejm/2017/0029-2665.

Hartman, P. and Perdok, W.G. (1955) On the relations between structure and morphology of crystals. I. Acta Crystallographica, 8, 49–52, https://doi.org/10.1107/S0365110X55000121.

Hem, J.D. (1978) Redox processes at surfaces of manganese oxide and their effects on aqueous metal ions. Chemical Geology, 21, 199–218, https://doi.org/10.1016/0009-2541(78)90045-1.

——— (1981) Rates of manganese oxidation in aqueous systems. Geochimica et Cosmochimica Acta, 45, 1369–1374, https://doi.org/10.1016/0016-7037(81)90229-5.

Hem, J.D., Roberson, C.E., and Fournier, R. (1982) Stability of βMnOOH and manganese oxide deposition from springwater. Water Resources Research, 18, 563–570, https://doi.org/10.1029/WR018i003p00563.

Ilton, E.S., Post, J.E., Heaney, P.J., Ling, F.T., and Kerisit, S.N. (2016) XPS determination of Mn oxidation states in Mn (hydr) oxides. Applied Surface Science, 366, 475–485, https://doi.org/10.1016/j.apsusc.2015.12.159.

Jarosch, D. (1987) Crystal structure refinement and reflectance measurements of hausmannite, Mn_3O_4. Mineralogy and Petrology, 37, 1523, https://doi.org/10.1007/BF01163155.

Klewicki, J.K. and Morgan, J.J. (1999) Dissolution of β-MnOOH particles by ligands: Pyrophosphate, ethylenediaminetetraacetate, and citrate. Geochimica et Cosmochimica Acta, 63, 3017–3024, https://doi.org/10.1016/S0016-7037(99)00229-X.

Kohler, T., Armbruster, T.A., and Libowitzky, E. (1997) Hydrogen bonding and Jahn–Teller distortion in groutite, α-MnOOH, and manganite, γ-MnOOH, and their relations to the manganese dioxides ramsdellite and pyrolusite. Journal of Solid State Chemistry, 133, 486–500, https://doi.org/10.1006/jssc.1997.7516.

Lefkowitz, J.P., Rouff, A.A., and Elzinga, E.J. (2013) Influence of pH on the reductive transformation of birnessite by aqueous Mn(II). Environmental Science & Technology, 47, 10364–10371, https://doi.org/10.1021/es402108d. PubMed

Luo, J., Segal, S.R., Wang, J.Y., Tian, Z.R., and Suib, S.L. (1996) Synthesis, characterization, and reactivity of feitknechtite. Proceedings of the Materials Research Society, 431, 3–8, https://doi.org/10.1557/PROC-431-3.

Luo, J., Huang, A., Park, S.H., Suib, S.L., and O'Young, C. (1998) Crystallization of Sodium-birnessite and accompanied phase transformation. Chemistry of Materials, 10, 1561–1568, https://doi.org/10.1021/cm970745c.

Mandernack, K.W., Post, J.E., and Tebo, B.M. (1995) Manganese mineral formation by bacterial spores of a marine Bacillus, strain SG-1: Evidence for the direct oxidation of Mn(II) to Mn(IV). Geochimica et Cosmochimica Acta, 59, 4393–4408, https://doi.org/10.1016/0016-7037(95)00298-E.

Meldau, R., Newesely, H., and Strunz, H. (1973) Zur kristallchemie von feitknechtite, β-MnOOH. Naturwissenschaften, 60, 387, https://doi.org/10.1007/BF00602514.

Novak, A. (1974) Hydrogen bonding in solids correlation of spectroscopic and crystallographic data. Structure and Bonding, 18, 177–216, https://doi.org/

10.1007/BFb0116438.
Özdemir, Ö. and Dunlop, D.J. (2000) Intermediate magnetite formation during dehydration of goethite. Earth and Planetary Science Letters, 177, 59–67, https://doi.org/10.1016/S0012-821X(00)00032-7.
Portehault, D., Cassaignon, S., Baudrin, E., and Jolivet, J. (2010) Evolution of nanostructured manganese (oxyhydr)oxides in water through MnO_4 reduction. Crystal Growth & Design, 10, 2168–2173, https://doi.org/10.1021/cg901394v.
Post, J.E. and Bish, D.L. (1989) Rietveld refinement of crystal structures using powder X-ray diffraction data. In D.L. Bish and J.E. Post, Eds., Modern Powder Diffraction, 20, 277–308. Reviews in Mineralogy. The Mineralogical Society of America.
Post, J.E. and Veblen, D.R. (1990) Crystal structure determinations of synthetic sodium, magnesium, and potassium birnessite using TEM and the Rietveld method. American Mineralogist, 75, 477–489.
Post, J.E., Heaney, P.J., and Hanson, J. (2002) Rietveld refinement of a triclinic structure for synthetic Na-birnessite using synchrotron powder diffraction data. Powder Diffraction, 17, 218–221, https://doi.org/10.1154/1.1498279.
Post, J.E., Heaney, P.J., and Ertl, A. (2008) Rietveld refinement of the ranciéite structure using synchrotron powder diffraction data. Powder Diffraction, 23, 10–14, https://doi.org/10.1154/1.2836477.
Prescher, C. and Prakapenka, V.B. (2015) DIOPTAS: A program for reduction of two-dimensional X-ray diffraction data and data exploration. High Pressure Research, 35, 223–230, https://doi.org/10.1080/08957959.2015.1059835.
Rietveld, H.M. (1969) A profile refinement method for nuclear and magnetic structures. Journal of Applied Crystallography, 2, 65–71, https://doi.org/10.1107/S0021889869006558.
Shannon, R.D. (1976) Revised effective ionic radii and systematic studies of interatomie distances in halides and chaleogenides. Acta Crystallographica, A32, 751–767, https://doi.org/10.1107/S0567739476001551.
Stephens, P.W. (1999) Phenomenological model of anisotropic peak broadening in powder diffraction. Journal of Applied Crystallography, 32, 281–289, https://doi.org/10.1107/S0021889898006001.
Thompson, P., Cox, D.E., and Hastings, J.B. (1987) Rietveld refinement of Debye-Scherrer synchrotron X-ray data from Al_2O_3. Journal of Applied Crystallography, 20, 79–83, https://doi.org/10.1107/S0021889887087090.
Toby, B.H. and Von Dreele, R.B. (2013) GSAS-II: The genesis of a modern open-source all purpose crystallography software package. Journal of Applied Crystallography, 46, 544–549, https://doi.org/10.1107/S0021889813003531.
Yamamoto, N., Horibe, M., and Higashi, S. (1981) Fourth polymorph of MnOOH; δ-MnOOH. Journal of the Japan Society of Powder and Powder Metallurgy, 28, 282–285, https://doi.org/10.2497/jjspm.28.282.
Yan, D., Li, Y., Liu, Y., Zhuo, R., Wu, R., and Wang, J. (2014) Growth mechanism and morphology control of porous hexagonal plates of hydrohausmannite prepared by hydrothermal method. Applied Mechanics and Materials, 513–517, 277–280, https://doi.org/10.4028/www.scientific.net/AMM.513-517.277.

Manuscript received July 26, 2022
Manuscript accepted December 6, 2022
Accepted manuscript online December 15, 2022
Manuscript handled by Lindsay P. Keller

Endnote:

[1]Deposit item AM-23-118729. Online Materials are free to all readers. Go online, via the table of contents or article view, and find the tab or link for supplemental materials.The CIF has been peer-reviewed by our Technical Editors.